

Origin of electronic Raman scattering and the Fano resonance in metallic carbon nanotubes

Eddwi H. Hasdeo^{1,*} Ahmad R. T. Nugraha¹,

Riichiro Saito¹, Kentaro Sato¹, and Mildred S. Dresselhaus^{2,3}

¹*Department of Physics, Tohoku University, Sendai 980-8578, Japan*

²*Department of Physics, Massachusetts Institute
of Technology, Cambridge, MA 02139-4307, USA*

³*Department of Electrical Engineering,
Massachusetts Institute of Technology, Cambridge, MA 02139-4307, USA*

(Dated: June 7, 2021)

Abstract

Fano resonance spectra for the G band in metallic carbon nanotubes are calculated as a function of laser excitation energy in which the origin of the resonance is given by an interference between the continuous electronic Raman spectra and the discrete phonon spectra. We found that the second-order scattering process of the $\mathbf{q} \neq 0$ electron-electron interaction is more relevant to the continuous spectra rather than the $\mathbf{q} = 0$ first-order process because the $\mathbf{q} = 0$ direct Coulomb interaction vanishes due to the symmetry of the two sublattices of a nanotube. We also show that the RBM spectra of metallic carbon nanotubes have an asymmetric line shape which previously had been overlooked.

PACS numbers: 78.67.Ch, 73.22.-f, 42.65.Dr, 03.65.Nk

Raman spectroscopy of single wall carbon nanotubes (SWNTs) and graphene has provided us with a better understanding of many optical properties which are very important for characterizing SWNTs and graphene not only for basic science understanding but also in applications [1]. Although most of the excitonic physics in the Raman spectra of SWNTs has been investigated intensively in terms of, for example, the excitation energy dependence (resonance Raman) [2, 3], chirality dependence (the Kataura plot) [4–6], Fermi energy dependence (the Kohn anomaly) [7–9], polarization dependence [10–12], and even strain dependence [13, 14], however, the asymmetric spectral shape of the G band for metallic SWNTs (m-SWNTs), also known as Breit-Wigner-Fano (BWF) line shape, is still not well explained theoretically. In a previous study, Brown *et al.* showed the diameter-dependent asymmetric spectral shape of the G band in which the asymmetric factor $1/q_{\text{BWF}}$ depends on the density of states at the Fermi energy [15]. Additionally, the BWF line shapes appear in graphite intercalation compounds (GICs) where $1/q_{\text{BWF}}$ depends on the staging number of GICs and thus also depends on the density of states at the Fermi energy [16]. Therefore, electrons in the gapless linear energy band of m-SWNTs should be expected to exhibit these asymmetry-related phenomena.

Fano pointed out that the asymmetric feature of a broadened spectrum comes from an interference between a discrete excitation spectrum and a continuum spectrum [17]. In m-SWNTs, electrons in the linear energy band play an important role to give rise to the continuum spectra and phonons give the discrete spectra. However, the detailed mechanism of the BWF line shapes in m-SWNTs remains a long-standing debatable topic. Some reports suggest that the coupling of a collective excitation (plasmon) with a phonon could explain the origin of the BWF asymmetry [15, 18–20], and some others argue that the single-particle electron-hole pair and phonon coupling via the Kohn anomaly is more relevant [21, 22]. Recently, Farhat *et al.* have observed a new feature of the continuum spectra exclusively in m-SWNTs which is ascribed to the electronic Raman scattering (ERS) [23]. The ERS feature (at $\sim 500 \text{ cm}^{-1}$) is observed in the energy region between the RBM and the G band and shows no phonon feature by the following arguments: (1) in comparison to the phonon spectral width ($\sim 1\text{-}50 \text{ cm}^{-1}$), the ERS width is much broader ($\sim 500 \text{ cm}^{-1}$) and has a smaller peak intensity ($I_{\text{ERS}} \approx 0.6I_{\text{G}}$), (2) the energy of the inelastic scattered light in the phonon Raman spectra is changed by changing the laser excitation energy E_{L} , while the ERS peak position does not change; it keeps constant at M_{ii} (i^{th} Van Hove singularity

transition energy), (3) the ERS feature is suppressed by changing the Fermi energy, which indicates that the origin of this spectrum comes from electron-hole pair excitations in the linear band of m-SWNTs by the Coulomb interaction.

In this Letter, we propose that the BWF feature of m-SWNTs comes from the interference between the G band and the ERS spectra. We calculate the exciton-exciton matrix elements of the Coulomb interaction which are responsible to give the ERS spectra. The exciton consideration is based on the fact that exciton effects in m-SWNTs are not negligible due to the one-dimensional carrier confinement even in the presence of the screening effect [24, 25]. The calculated results of the present work suggest that the zero momentum transfer ($\mathbf{q} = 0$) vanishes in the direct Coulomb interaction because of the symmetry of the wave-function, and thus a higher order Raman process is more relevant to the ERS. By considering the second-order Raman process, we are able to reproduce experimental results of the ERS spectra consistently. We will also show that the RBM spectra of m-SWNTs have a similar asymmetric line shape, indicating that the ERS can be coupled with both the G band and the RBM.

Optical processes of the ERS consist of (i) an exciton generation via an exciton-photon interaction, (ii) excitation of another exciton in the linear energy band by the Coulomb interaction with the photo-excited exciton, and (iii) finally the photo-excited exciton goes back to the ground state by emitting a photon. The exciton-exciton interaction in (ii) may occur in a first-order or high-order process. Here, we consider up to second-order processes for simplicity. For the first-order process, the photo-excited exciton relaxes vertically ($\mathbf{q} = 0$) from a virtual state Ψ^{vir} to the M_{ii} state after photo-absorption at a wave vector \mathbf{k} , while the other exciton is created in the linear band at wave vector \mathbf{k}' by the Coulomb interaction (see Fig. 1(a)). In the second-order process, on the other hand, the existence of the two inequivalent \mathbf{K} and \mathbf{K}' points in the graphene Brillouin zone leads to two different scattering processes, i.e. *intra-valley* (AV) scattering and the *inter-valley* (EV) scattering, shown in Figs. 1(b) and (c), respectively. In both cases, two excitons are excited at the linear band. For each scattering process, we also have two cases where the two electrons at parabolic and linear bands may exist in the same valley (*A* state), or they may exist in the different valleys (*E* state). Such a symmetry labeling for *A* and *E* states is obtained from the group theory. After going through the electronic scattering process, the photo-excited exciton then returns to the ground state by emitting a photon with resonance energy $E_s = M_{ii}$. This is

the reason why the ERS peak remains at M_{ii} even though we change the laser energy E_L .

Considering all the processes shown in Fig. 1, we write the perturbed Hamiltonian as:

$$H_{e-e} = \sum_{\mathbf{k}, \mathbf{k}', \mathbf{q}} W^{(\pm)} \left((\mathbf{k} + \mathbf{q}), (\mathbf{k}' - \mathbf{q}), \mathbf{k}, \mathbf{k}' \right) \times c_{\mathbf{k}+\mathbf{q}}^{\dagger c} c_{\mathbf{k}'-\mathbf{q}}^{\dagger c'} c_{\mathbf{k}'}^{v'} c_{\mathbf{k}}^c, \quad (1)$$

where \mathbf{k} and \mathbf{k}' denote, respectively, an electron state in the parabolic and the linear band, while $c_{\mathbf{k}}^{\dagger c} (c_{\mathbf{k}}^v)$ is the creation (annihilation) operator in the conduction (valence) band. The direct (exchange) interaction K^d (K^x) contributes to the two-body Coulomb interaction W as follows: $W^{(\pm)} = K^d \pm K^x$, in which $+$ ($-$) gives a singlet (triplet) state for the two electrons. K^d and K^x are expressed as [26]:

$$K^d = \sum_{ss'=A,B} C_{s,\mathbf{k}+\mathbf{q}}^{c*} C_{s',\mathbf{k}'-\mathbf{q}}^{c*} C_{s,\mathbf{k}}^c C_{s',\mathbf{k}'}^v \times \Re(w_{ss'}(\mathbf{q})), \quad (2)$$

$$K^x = \sum_{ss'=A,B} C_{s,\mathbf{k}+\mathbf{q}}^{c*} C_{s',\mathbf{k}'-\mathbf{q}}^{c*} C_{s',\mathbf{k}}^c C_{s,\mathbf{k}'}^v \times \Re(w_{ss'}(\mathbf{k}' - \mathbf{k} - \mathbf{q})), \quad (3)$$

where $C_{s,\mathbf{k}}^{c(v)}$ are the tight binding coefficients for $s = A, B$ atomic sites of the conduction (valence) band, $\Re()$ is the real part of a complex variable, and the screened potential $w(\mathbf{q})$ is given by the random phase approximation (RPA): $w(\mathbf{q}) = v(\mathbf{q})/\kappa(1 + v(\mathbf{q})\Pi(\mathbf{q}))$ [6, 12]. Here $v(\mathbf{q})$ denotes the Fourier transform of the Ohno potential, $\Pi(\mathbf{q})$ is the RPA polarization function, and κ is the static dielectric constant due to electronic core states, σ bands, and the surrounding material. In this calculation we used a constant $\kappa = 2.2$ [6].

The exciton-exciton matrix element for the photo-excited exciton and another exciton in a linear energy band is calculated using the following formula:

$$\begin{aligned} \mathcal{M}_{\text{ex-ex}}^{\pm}(\mathbf{q}) &= \langle \Psi^f | H_{e-e} | \Psi^{\text{vir}} \rangle \\ &= \sum_{\mathbf{k}, \mathbf{k}'} Z_{(\mathbf{k}+\mathbf{q})c, \mathbf{k}v}^* Z_{(\mathbf{k}'-\mathbf{q})c, \mathbf{k}'v}^* Z_{\mathbf{k}c, \mathbf{k}v} \\ &\quad \times W^{(\pm)} \left((\mathbf{k} + \mathbf{q}), (\mathbf{k}' - \mathbf{q}), \mathbf{k}, \mathbf{k}' \right). \end{aligned} \quad (4)$$

Here the photo-excited exciton state is defined by:

$$|\Psi^{\text{vir}}\rangle = \sum_{n, \mathbf{k}} Z_{\mathbf{k}c, \mathbf{k}v}^n c_{\mathbf{k}}^{\dagger c} c_{\mathbf{k}}^v |g\rangle, \quad (5)$$

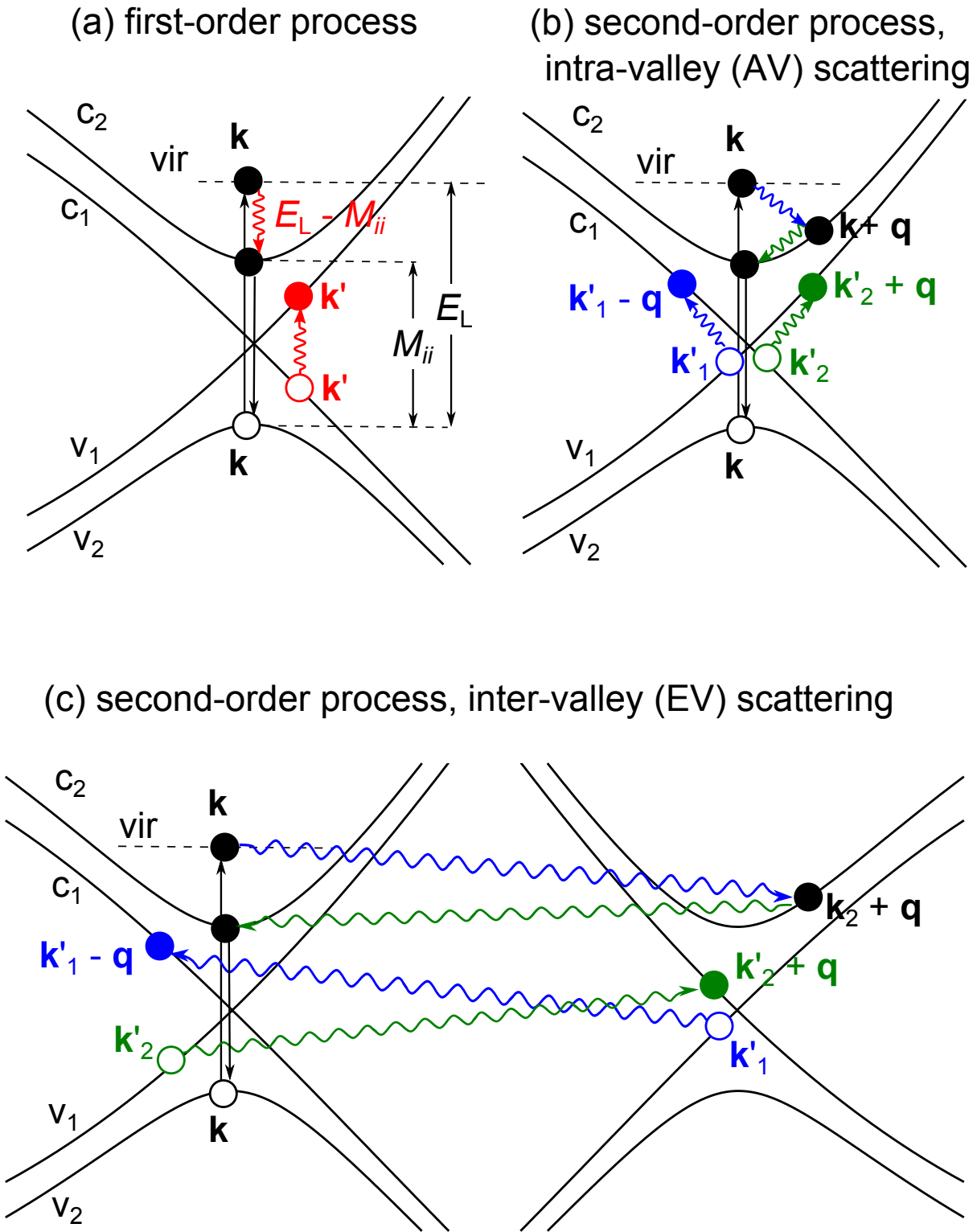


Figure 1: (Color online) (a) First-order electronic Raman process. (b) AV and (c) EV second-order scattering processes ($\mathbf{q} \neq 0$). In both the first-order and second-order processes, the interaction between electrons in the parabolic band and the linear band can take place in the same valley (\mathbf{K} or \mathbf{K}') or in a different valley.

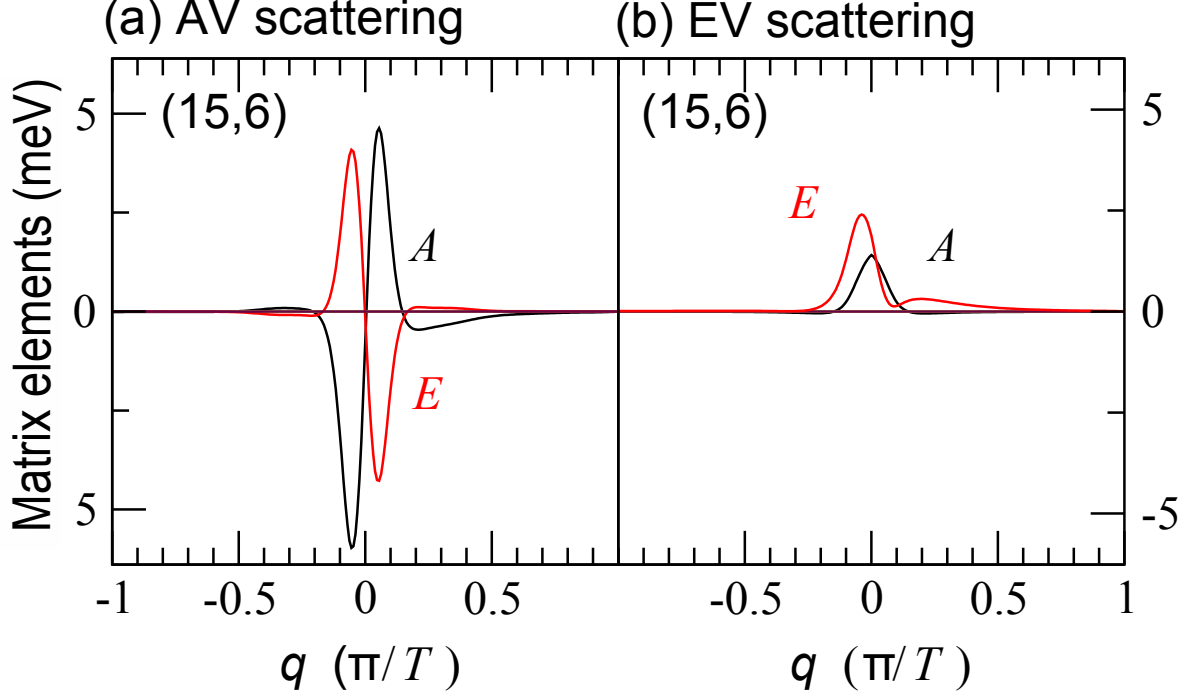


Figure 2: (Color online) Singlet state exciton-exciton matrix elements $\mathcal{M}_{\text{ex-ex}}^+$ calculated for a (15,6) tube with a diameter of 1.46 nm. Panel (a) is for the intra-valley scattering and (b) is for the inter-valley scattering. Label A (E) inside each panel shows the A (E) states, in which two electrons lie in the same (different) valley. The wave vector \mathbf{q} is projected on the one-dimensional SWNT cutting lines and expressed in terms of the translational vector length T . We have $T = 0.89$ nm for the (15,6) tube.

where $Z_{\mathbf{k}_c, \mathbf{k}_v}^{n*}$ is the eigenvector of n -th exciton state solved from the Bethe-Salpeter equation, \mathbf{k}_c and \mathbf{k}_v denote wave vectors for the electron and hole states, respectively, with $\mathbf{k}_c = \mathbf{k}_v$ for a bright exciton, and $|g\rangle$ denotes the ground state [6]. In Eq. (5), we only use the lowest exciton state $n = 0$, since it gives the dominant value to the exciton-photon matrix element [27]. The final state of Eq. (4) is given by:

$$|\Psi^f\rangle = \sum_{\mathbf{k}, \mathbf{k}'} Z_{(\mathbf{k}+\mathbf{q})c, \mathbf{k}_v} Z_{(\mathbf{k}'-\mathbf{q})c, \mathbf{k}'_v} c_{\mathbf{k}+\mathbf{q}}^{\dagger c} c_{\mathbf{k}'-\mathbf{q}}^{\dagger c} c_{\mathbf{k}'}^v c_{\mathbf{k}}^v |g\rangle. \quad (6)$$

In Fig. 2, we show the calculated exciton-exciton matrix elements for singlet states $\mathcal{M}_{\text{ex-ex}}^+$ in a (15,6) m-SWNT. It is noted that the matrix elements for the triplet states $\mathcal{M}_{\text{ex-ex}}^-$ are comparable with those for the singlet states, so here we only show the singlet state case. Surprisingly, the AV scattering matrix elements give almost a zero value at $\mathbf{q} = 0$ for both A

and E states, as shown in Fig. 2(a). In fact, we find that the direct interaction K^d vanishes at $\mathbf{q} = 0$ for all nanotubes. At $\mathbf{q} = 0$, only the exchange interaction K^x gives a small contribution from the AV scattering. The vanishing K^d can be explained by the presence of three C_s^c and one C_s^v coefficients in Eq. (2). The product of wave functions always gives an opposite sign when we exchange $A \rightarrow B$ in s or s' and thus the total summation over A and B sublattices vanishes at $\mathbf{q} = 0$ [26]. As long as we incorporate three C^c and one C^v coefficients into K^d , the vanishing direct Coulomb interaction at $\mathbf{q} = 0$ is a general phenomenon in graphene and SWNTs systems. Furthermore, the EV scattering matrix elements shown in Fig. 2(b) are an even function of q because C^c and C^v change their signs by exchanging \mathbf{K} and \mathbf{K}' in the B sublattice, while in the A sublattice there are no changes in sign for C^c and C^v . The results from Figs. 2(a) and (b) thus imply that the first-order Raman process corresponding to the AV scattering at $\mathbf{q} = 0$ as shown in Fig. 2(a) makes only a minor contribution to the Raman spectra. Consequently, we should consider the second-order ERS process, in which the $\mathbf{q} \neq 0$ term in Fig. 2(a) becomes important.

Next, to explain the Fano resonance in m-SWNTs, we calculate the Raman intensity by taking into account each contribution from the RBM, ERS, and G band, and considering all possible initial (i) and final (f) states:

$$I = \sum_i \left| \sum_f (A_{\text{RBM}} + A_{\text{ERS}} + A_{\text{G}}) \right|^2, \quad (7)$$

in which we have A_{RBM} and A_{G} for the phonon spectral amplitudes and A_{ERS} for the electronic scattering amplitude. We do not consider the G' band because its position ($\sim 2700 \text{ cm}^{-1}$) is quite far from the ERS and might not interfere with the ERS as indicated in Farhat's experiment (Fig. 3(b)). The amplitude of each phonon spectrum can be calculated by:

$$A_\nu(\omega_s) = \frac{1}{\pi} \sum_{n,n'} \left[\frac{\mathcal{M}_{\text{ex-op}}^{n,i}}{[\Delta E_{ni} - i\gamma]} \frac{\mathcal{M}_{\text{ex-ph}}^{n',n}}{[\Delta E_{n'i} - \hbar\omega_\nu - i(\gamma + \Gamma_\nu)]} \right. \\ \left. \times \frac{\mathcal{M}_{\text{ex-op}}^{f,n'}}{[E_L - \hbar\omega_\nu - \hbar\omega_s - i\Gamma_\nu]} \right], \quad (8)$$

where $\nu = \text{RBM or G mode}$, $\Delta E_{mi} = E_L - E_m - E_i$, and $\hbar\omega_s$ is the scattered photon energy. We use a broadening factor $\gamma = 60 \text{ meV}$ for the life time of the photo-excited carriers [28]. We also utilize the phonon spectral width for the RBM as a constant $\Gamma_{\text{RBM}} = 10 \text{ cm}^{-1}$,

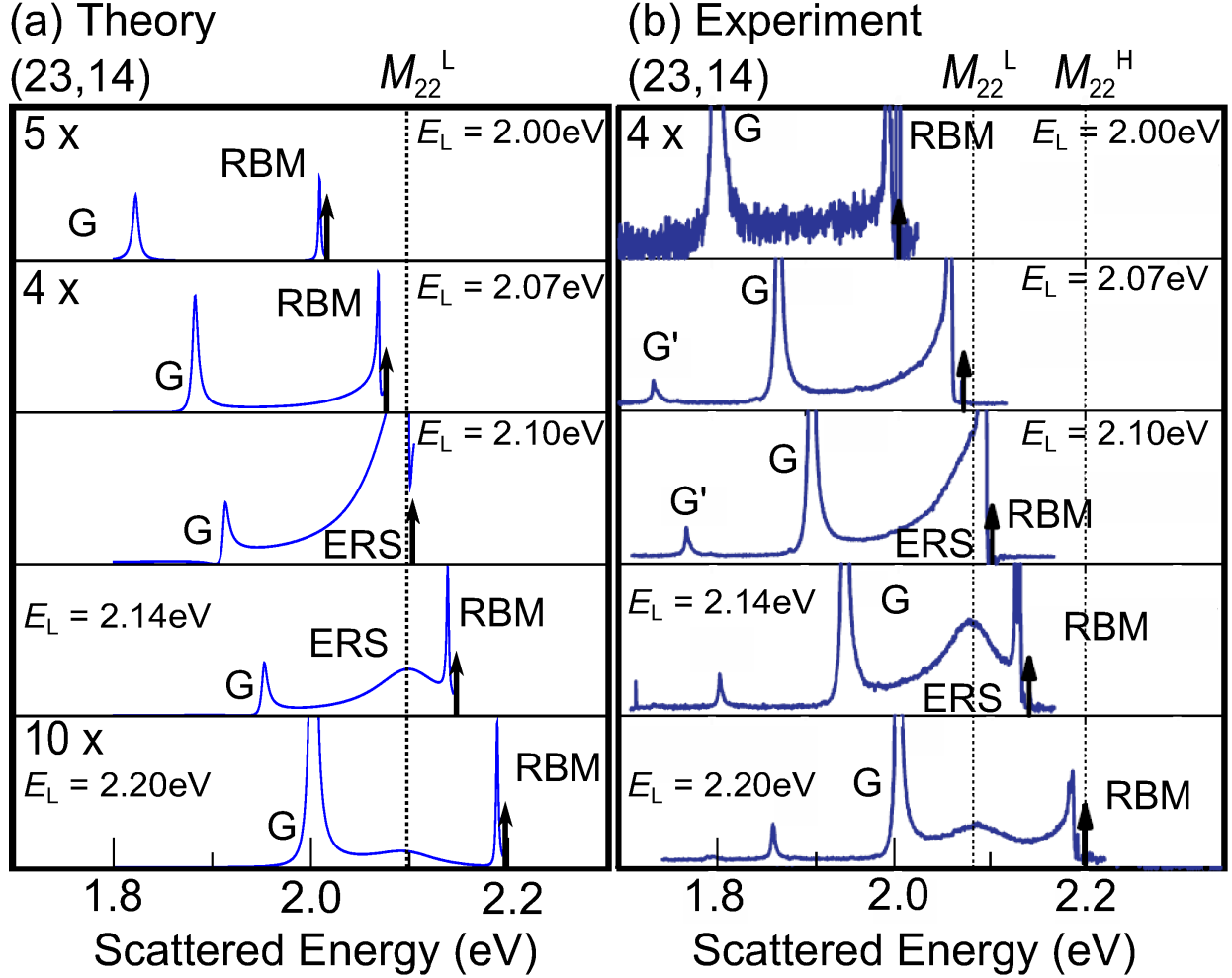


Figure 3: (Color online) (a) Calculated result (this work) and (b) experimental results (adapted from Ref. [23]) of Raman intensity versus scattered photon energy ($\hbar\omega_s$) for a (23,14) tube where we have the calculated $M_{22}^L = 2.10$ eV and the experimental $M_{22}^L = 2.08$ eV. The laser excitation energies E_L are taken as 2.00, 2.07, 2.10, 2.14, and 2.20 eV.

and for the G band, which consist of in-plane transverse optic (iTO) $\Gamma_{iTO} = 20$ cm^{-1} and longitudinal optic (LO) $\Gamma_{LO} = 31$ cm^{-1} [21]. The exciton-photon ($\mathcal{M}_{\text{ex-op}}^{b,a}$) and exciton-phonon ($\mathcal{M}_{\text{ex-ph}}^{b,a}$) matrix elements for a transition between states $a \rightarrow b$ are taken from Jiang's work [27]. We approximate the virtual states $i = f$ and $n = n'$. On the other hand,

the amplitude of the second-order ERS process is given by:

$$\begin{aligned}
A_{\text{ERS}}(\omega_s) = & \frac{1}{\pi} \sum_{n,n',n'',\sigma} \left[\frac{\mathcal{M}_{\text{ex-op}}^{n,i}}{[\Delta E_{ni} - i\gamma]} \right. \\
& \times \frac{\mathcal{M}_{\text{ex-ex}}^{n',n}(q)}{[\Delta E_{n'i} - \hbar\omega_1 - i(\gamma + \Gamma_x)]} \\
& \times \frac{\mathcal{M}_{\text{ex-ex}}^{n'',n'}(-q)}{[\Delta E_{n''i} - \hbar\omega_1 - \hbar\omega_2 - i(\gamma + 2\Gamma_x)]} \\
& \left. \times \frac{\mathcal{M}_{\text{ex-op}}^{f,n'}}{[E_L - \hbar\omega_1 - \hbar\omega_2 - \hbar\omega_s - 2i\Gamma_x]} \right], \tag{9}
\end{aligned}$$

where we also consider the same virtual state approximation as in Eq. (8). Here, ω_1 and ω_2 are the energies of the linear band excitons emitted from the exciton-exciton interaction in the second-order ERS process. The summation over σ denotes all different processes in the ERS mechanism, i.e. AV and EV scattering processes. The electron-electron interaction life time is set at a constant value $\Gamma_x = 25$ meV.

In Fig. 3(a) we show the calculated result of the E_L dependence of the Raman intensity as a function of scattered photon energy ($\hbar\omega_s$). In the present work, we only calculate the E_L dependence of the Raman intensity near M_{22}^L . Despite the two contributions from the LO and iTO phonon vibrations for the G mode, the splitting of the G^+ and G^- modes do not appear visibly in the spectra due to the large diameter of the (23,14) tube ($d_t = 2.5$ nm) which makes it has a small curvature effect. Even though we can not reproduce the relative intensity scale exactly from the experimental data, our calculated result can explain the behavior of the observed ERS as shown in Fig. 3(b). The ERS feature has a very broad spectral width ($\text{FWHM}^{\text{ERS}} \approx 50$ meV) with a peak intensity almost comparable to that of the RBM. Unlike the other phonon modes, whose peak positions are shifted by changing E_L , the ERS peak remains at the frequency of the M_{ii} transition. At $E_L = 2.07$ eV, the ERS spectrum starts to appear and modifies the RBM and the G band line shapes. At that point, although E_L is 30 meV below M_{ii} , the energy-momentum conservation during the exciton-exciton scattering may be violated by the Heisenberg uncertainty principle ($\Delta t \approx 10$ fs corresponding to $\Delta E \approx 100$ meV).

Each Raman intensity calculated from Eq. (7) actually gives a Lorentzian shape for all phonon modes and also for the ERS as presented in Fig. 4(a). However, the broad feature of the ERS overlaps with the phonon modes and thus the interference between them gives rise to the asymmetric line shape, peak shifting, and the enhancement of both the RBM

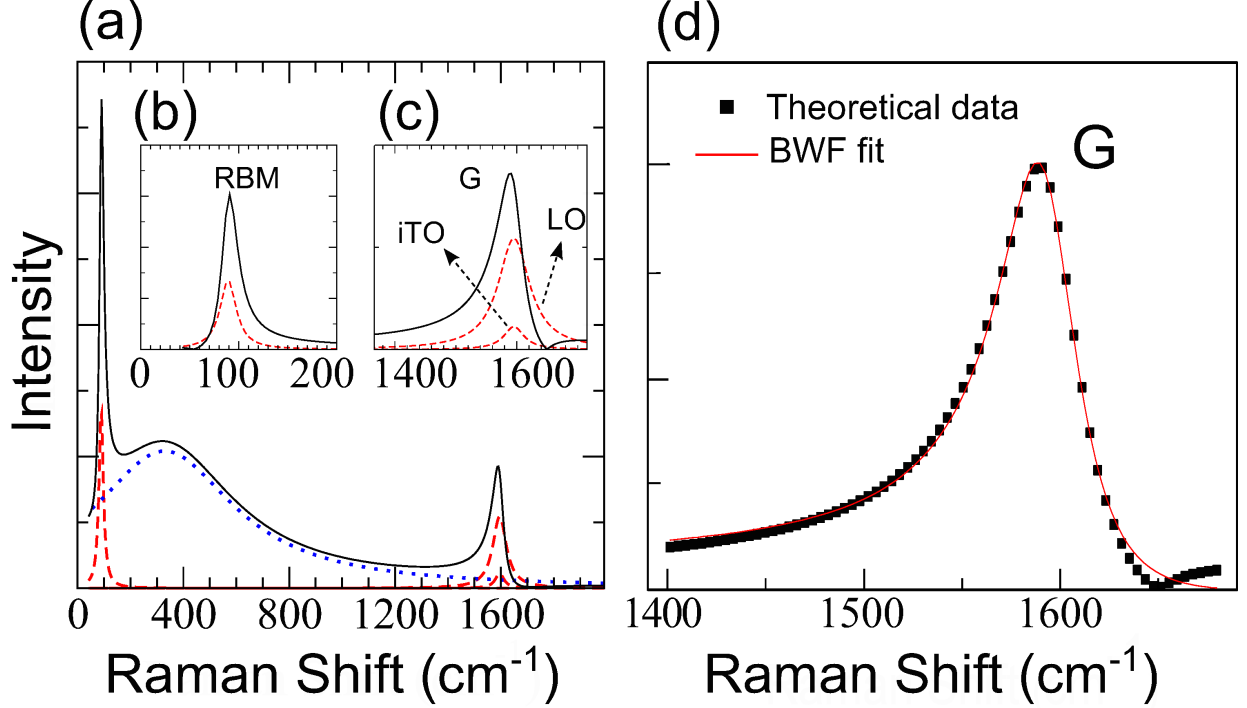


Figure 4: (Color online) Calculated Raman spectra for a (23,14) SWNT with $E_L = 2.14$ eV. The total intensity shown in panel (a) is represented by the solid line. The dashed lines show contributions from the RBM and G modes, while the dotted blue line is the contribution from the ERS. Each line shape for the RBM, the G modes, and the ERS are Lorentzian. (b) The RBM and (c) the G band spectra after subtracting the ERS spectrum. The dashed lines are identical with those in (a). (d) Fitting result of the G band spectrum to the BWF line shape of Eq. (10). Filled squares are calculated results and the solid line shows the BWF fitting.

and the G bands, which can be seen in Figs. 4(b) and (c). We find that the asymmetric line shape of the G band after subtracting the ERS contribution clearly shows the BWF line shape (Fig. 4(d)), fitted by

$$I(\omega) = I_0 \frac{[1 + (\omega - \omega_0)/q_{\text{BWF}}\Gamma]^2}{1 + [(\omega - \omega_0)/\Gamma]^2}, \quad (10)$$

where q_{BWF} , Γ , and ω_0 are parameters to be determined. From this fitting, we can find and analyze the E_L dependence of the asymmetric factor $1/q_{\text{BWF}}$, the spectral width Γ , and the peak position ω_0 (see Fig. 5). According to Fano [17], $1/q_{\text{BWF}}$ is proportional to the coupling constant between the continuum spectrum and the discrete spectrum. In our case, $|1/q_{\text{BWF}}|$ (FWHM or ω_0) as a function of resonance condition $E_L - M_{22}^L$ has a “ Λ ” (“V”)

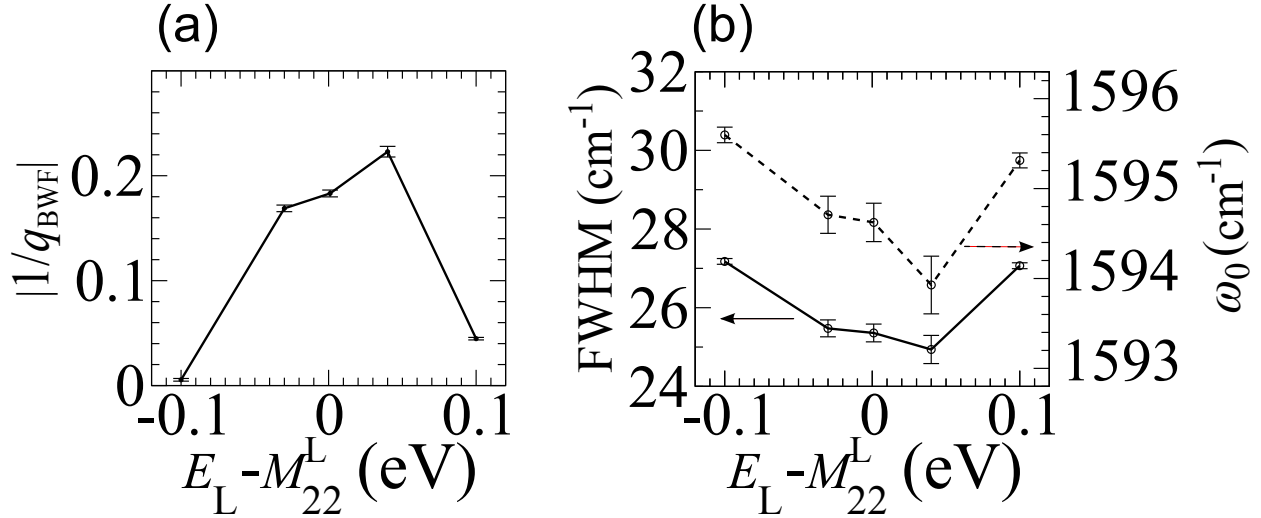


Figure 5: (a) Asymmetric factor ($1/q_{\text{BWF}}$), and (b) spectral width and peak position of the G band as a function of resonance condition for the (23,14) tube. The solid and dashed arrows are given as a guide for the corresponding axes. .

shape, with the maximum (minimum) peak ~ 40 meV above the resonance as depicted in Fig. 5(a)(Fig. 5(b)). $|1/q_{\text{BWF}}|$ reaches a maximum value because the intensity and the peak position of the ERS allows it to have a very strong overlap with the G band at that point. This coupling also induces the narrowing and the shifting of the G band peak closer to the ERS peak position.

From our theoretical point of view, we suggest some conditions how the ERS and asymmetric phonon modes in m-SWNTs can be observed experimentally. Since the Coulomb interaction is inversely proportional to the SWNT diameter d_t and also sense a curvature-induced band gap ($\sim \cos \theta/d_t^2$ meV) appears for small chiral angles θ for $d_t < 1$ nm [29], the diameter range of m-SWNTs which allows us to observe the ERS and Fano resonance should be around 1 – 2 nm. Moreover, the finite length of m-SWNTs leads to discrete k points and the electron-electron interaction energy is around 60 meV; thus the nanotube length should be larger than $4 \mu\text{m}$ for 1 meV energy resolution. The energy of the second-order exciton-exciton interaction ($\hbar\omega_1$) is only ~ 10 meV lower than the first-order process because the linear band slope is steeper than that for the parabolic band. Therefore, in order to identify the dominant contribution of the second-order process, the low temperature (10 – 100 K) gate voltage experiment must be performed.

In summary, we have formulated a theoretical picture of the ERS by considering the exciton-exciton interaction. We showed that the non-zero momentum transfer process $\mathbf{q} \neq 0$ gives a dominant contribution to the ERS spectra. This ERS spectrum is strongly coupled with the G band and the RBM and the interference with the ERS spectrum modifies the line shapes of the two phonon modes which results in these phonon modes having the BWF line shapes. The asymmetry, narrowing, and shifting of the G band induced by interference with the ERS are all sensitive to the peak intensity ratio and the peak distance between the ERS and the G band. The RBM mode also is predicted to have a similar asymmetry which opens up the possibility for future experimental observations and clarifications.

E.H. and A.R.T.N. are supported by a MEXT scholarship. R.S. and K.S. acknowledge MEXT grant Nos. 20241023 and 23710118, respectively. M.S.D. acknowledges NSF-DMR grant No. 10-04147.

* E-mail: hasdeo@flex.phys.tohoku.ac.jp

- [1] R. Saito et al., *Advances in Physics* **60**, 413 (2011).
- [2] A. Jorio et al., *Phys. Rev. Lett.* **86**, 1118 (2001).
- [3] A. M. Pimenta et al., *J. Mater. Res.* **13**, 2396 (1998).
- [4] H. Kataura et al., *Synthetic Metals* **103**, 2555 (1999).
- [5] R. Saito, et al., *Phys. Rev. B* **61**, 2981 (2000).
- [6] J. Jiang et al., *Phys. Rev. B* **75**, 035407 (2007).
- [7] H. Farhat et al., *Phys. Rev. Lett.* **99**, 145506 (2007).
- [8] K. Sasaki et al., *Phys. Rev. B* **78**, 235405 (2008).
- [9] J. S. Park et al., *Phys. Rev. B* **80**, 081402 (2009).
- [10] S. Uryu and T. Ando, *Phys. Rev. B* **74**, 155411 (2006).
- [11] Y. Miyauchi, et al., *Phys. Rev. B* **74**, 205440 (2006).
- [12] A. Grüneis et al., *Phys. Rev. B* **67**, 165402 (2003).
- [13] L. Li, et al., *Carbon* **49**, 4412 (2011).
- [14] S. B. Cronin et al., *Phys. Rev. B* **72**, 035425 (2005).
- [15] S. D. M. Brown et al., *Phys. Rev. B* **63**, 155414 (2001).
- [16] P. C. Eklund, et al., *Phys. Rev. B* **16**, 3330 (1977).

- [17] U. Fano, Phys. Rev. **124**, 1866 (1961).
- [18] S. M. Bose, et al., Phys. Rev. B **72**, 153402 (2005).
- [19] C. Jiang et al., Phys. Rev. B **66**, 161404 (2002).
- [20] K. Kempa, Phys. Rev. B **66**, 195406 (2002).
- [21] M. Lazzeri, et al., Phys. Rev. B **73**, 155426 (2006).
- [22] Y. Wu et al., Phys. Rev. Lett. **99**, 027402 (2007).
- [23] H. Farhat et al., Phys. Rev. Lett. **107**, 157401 (2011).
- [24] F. Wang et al., Phys. Rev. Lett. **99**, 227401 (2007).
- [25] C. D. Spataru, et al., Phys. Rev. Lett. **92**, 077402 (2004).
- [26] See Supplemental Material at [link provided by APS] for a detailed derivation of electron-electron interaction matrix elements.
- [27] J. Jiang et al., Phys. Rev. B **75**, 035405 (2007).
- [28] K. Sato, et al., Chem. Phys. Lett. **497**, 94 (2010).
- [29] M. Ouyang, et al., Science **292**, 702 (2001).